

# A COMPARISON OF THE EUV AND X-RAY EMISSION PROFILES IN SIX CLUSTERS OF GALAXIES

Florence DURRET

*Institut d'Astrophysique de Paris, 98bis Bd Arago, 75014 Paris, France*

Sergio DOS SANTOS

*Department of Physics and Astronomy, Leicester University, University Road, Leicester LE1 7RH, UK*

Richard LIEU

*Department of Physics, University of Alabama, Huntsville AL 35899, USA*

We have performed the wavelet analysis and image reconstructions for six clusters of galaxies observed both at extreme ultraviolet and X-ray energies. The comparison of the profiles of the EUV and X-ray reconstructed images shows that they differ at a very large confidence level in five of the six clusters, and are similar only for the Coma cluster, which is by far the hottest one in the sample.

## 1 Introduction

The Extreme Ultraviolet Explorer (EUVE) has detected emission from a few clusters of galaxies in the 70-200 eV energy range. By order of discovery, these are: Coma (Lieu et al., 1996a), Virgo (Lieu et al., 1996b; Berghöfer et al., 2000a), A 1795 (Mittaz et al., 1998), A 2199 (Bowyer et al., 1998), A 4059 (Berghöfer et al., 2000b) and Fornax (Berghöfer, Bowyer & Korpela 2001). The problem of the physical origin of the EUV emission was immediately raised. Excess EUV emission relative to the extrapolation of the X-ray emission to the EUVE energy range was detected in several clusters, suggesting that thermal bremsstrahlung from the hot (several  $10^7$  to  $10^8$ K) gas emitting in X-rays could not be entirely responsible for the EUV emission. However, the reality and importance of this effect is still controversial.

This excess UV emission has been interpreted as due to two different mechanisms: thermal radiation from a warm ( $10^5 - 10^6$ K) gas, as first suggested by Lieu et al. (1996a), or inverse Compton emission of relativistic electrons either on the cosmic microwave background or on stellar light originating in elliptical galaxies (Bowyer & Berghöfer, 1998; Sarazin & Lieu, 1998). Although the existence of a multiphase intracluster medium is likely (Bonamente et al., 2001; Lieu et al., 2001), there are several difficulties with the thermal model. The most serious one is that since gas in the temperature range  $10^5 - 10^6$ K cools very rapidly, a source of heating (and refuelling) for this gas is necessary, and no satisfactory model has been proposed until now to account for the gas heating. On the other hand, non thermal models (Sarazin & Lieu, 1998; Bowyer & Berghöfer, 1998; Lieu et al., 1999b; Enßlin et al., 1999; Atoyan & Völk, 2000; Brunetti et al., 2001) seem able to account for the excess EUV emission, but still require some fine tuning.

We have performed for a sample of six clusters a wavelet analysis and reconstruction of the EUVE and ROSAT (PSPC for five of them and ROSAT HRI for A 4038) images. We compare the profiles of the images thus obtained, arguing that if both emissions have the same physical origin the profiles should be identical.

## 2 The data and data analysis

### 2.1 The data

Observations in the EUV range were made with the EUVE satellite. The ROSAT data were retrieved from the archive. The exposure times and main cluster characteristics are given in Table 1.

Table 1: Exposure times and main cluster characteristics.

Cluster	EUVE total exp. time (s)	ROSAT exp. time (s)	ROSAT ObsId	Redshift	$kT_X$ (keV)	Scaling (kpc/superpx)	Cooling flow
A 1795	158689	33921	rp800105	0.063	5.9	32.7	yes
A 2199	93721	34633	rp800644	0.0299	4.1	15.8	yes
A 4038	161492	11480	rh800962	0.0283	4.0	14.9	yes
A 4059	145389	5225	rp800175	0.0478	4.0	25.0	yes
Virgo	146204	9135	rp800187	0.003	2.4	1.6	weak
Coma	60822	20112	rp800005	0.023	8.7	12.2	no

In order to have comparable spatial resolutions in the EUV and X-rays, the EUV images were rebinned  $4 \times 4$ , leading to a “superpixel” size of 0.307 arcminutes (18.4 arcseconds). Reduced X-ray images were also rebinned (from 15 arcsec pixels for the PSPC and 5 arcsec pixels for the HRI) to the same 18.4 arcsec pixel size in order to allow a direct comparison of the EUV and X-ray profiles.

The linear scale at the cluster distance per superpixel, estimated with  $H_0 = 50 \text{ km s}^{-1} \text{ Mpc}^{-1}$  and  $q_0=0$  is given in column 7 of Table 1.

### 2.2 Data reduction

The ROSAT X-ray data for each cluster were obtained from the HEASARC web archive<sup>a</sup>. Because of its higher sensitivity, we privileged, when possible, PSPC data over HRI and pointed observations over all-sky survey scanning mode observation. When multiple PSPC observations were available, we always used the one with the smallest offset radius compared to the center of the cluster, and the longest exposure.

The ROSAT PSPC data were reduced with S. Snowden’s Extended source Analysis Software. We limited our analysis to the [0.5,2.0] keV energy band (bands R4-R7 as defined in Snowden et al., 1994). This preliminary reduction produced a surface brightness image with  $512 \times 512$  pixels, 15 arcsec per pixel (roughly the FWHM of the PSPC PSF at 1keV), as well as an exposure image for each of the bands and a background image.

The ROSAT HRI data for A4038 were reduced with the same ESAS package, leading to an image of  $512 \times 512$  pixels with 5 arcsec per pixel.

The EUVE/Deep Survey photometer (DS) images were extracted from the raw event lists with the customary linear bin size of 13 pix/arcmin. The rectangular shape of the Lex/B filter ( $\sim 70\text{-}200 \text{ eV}$ ) results in highly elongated images (see Fig. 2). When more than one observation

<sup>a</sup><http://heasarc.gsfc.nasa.gov/>

was available for each target, images were coadded to improve the S/N; the rectangular shape often results in only partial overlap between the exposures (e.g. Fig. 3).

### 2.3 The wavelet transform

The detailed method and its tests on simulated and real images will be presented elsewhere (Dos Santos et al., in preparation). Here, we will only highlight the different steps.

The wavelet transform (hereafter WT) has proven its capabilities in numerous astronomical applications, such as the detection of the large scale structure (e.g. Slezak 1993), galaxy detections and counts (Slezak et al., 1990), reconstruction of cluster X-ray images (Slezak et al., 1994) and structure detection in low intensity X-ray images (e.g. Dos Santos & Mamon 1999). We used the *à trous* discrete wavelet algorithm (Shensa, 1992), implemented in a package kindly provided by E. Slezak. In the *à trous* implementation of the WT, an  $N \times N$  image is transformed into  $P$  wavelet planes (hereafter WP), each being the difference between two consecutive wavelet convolutions at scales  $i$  and  $i + 1$  (with  $2^i$  and  $2^{i+1}$  pixels respectively, with  $1 \leq i \leq P$ ). The pixel values in the plane  $i$  are called the wavelet coefficients at scale  $i$ . The main advantage of this algorithm is that each WP has the same number of pixels as the initial image, and thus, the reconstruction of the image (for example after thresholding in the WPs) is a straightforward addition process.

The noise estimation in the WPs is the main difficulty of the reconstruction process. Once the noise in the WPs has been estimated, it is straightforward to identify the wavelet coefficients which are statistically significant at a certain level. These coefficients are left unchanged, while all the others are replaced by zero (this process is often called “hard thresholding”). Then a simple addition of the thresholded WPs gives what is called the denoised image, which will be used for scientific analysis.

### 2.4 Estimation of the noise in the Wavelet Planes

For an image with a stationary gaussian white noise, the resulting noise in each WP is itself gaussian, and its standard deviation can be computed analytically, once the resultant of a gaussian noise of standard deviation 1 has been computed on each WP (see e.g. Rué, 1996).

For Poisson noise, techniques of variance stabilization have been introduced, which work under the assumption that the mean value of the image is large (typically, more than 30 counts per pixel, see Murtagh et al., 1995). However, for very low counts (typically less than 10), this Anscombe transform (Anscombe, 1948) loses control over the bias. In this case, an alternative approach is needed.

We have adopted a new method for the noise evaluation in each WP. The complete method will be presented elsewhere (Dos Santos et al., in preparation), and we only outline the important features here.

Basically, what we want to assess is the probability that a certain wavelet coefficient  $c_i(x, y)$  (at scale  $i$  and position  $(x, y)$ ) is due to noise. We first consider an initial image which is zero-valued everywhere, except on its central pixel, where its value is  $p(x_0, y_0)$  (the translation invariance property of the wavelet transform ensures that choosing the central pixel has no consequences on the generality of the reasoning). After the wavelet transform of the image, this single pixel will have a non-vanishing contribution on each of the WPs. Of course, since the wavelet function has a finite support, the contribution of this single pixel outside this support will be zero. Suppose now that we have an estimation of the noise level on this particular pixel. This estimation is  $n(x_0, y_0)$ . We can then simulate an image with, say, Poisson noise (or whatever noise process we choose) of mean  $n$  and apply to it the wavelet transform. Looking at the histogram of each WP of the simulated image in turn, we can measure the minimum threshold  $n_i$  that ensures that a fraction  $F$  of the wavelet coefficient pixels of plane  $i$  have a

value lower than  $n_i$ . In other words, a value of a pixel in the WP  $i$  will have a probability  $F$  to be *lower* than  $n_i$  (or a probability  $1-F$  to have a value *higher* than  $n_i$ ). Now returning to the initial image and its wavelet transform, we can compare the value of each wavelet coefficient in plane  $i$  with this threshold  $n_i$ . If this value is higher, its probability of not being due to noise is  $1-F$  and we keep it. If it is lower, we don't keep it and put its value to zero. We do this in turn for each WP. Since the pixels are considered as independent, we can repeat the same simulation and the same thresholding on each pixel of an image (which has got many non-zero valued pixels this time). Having an estimation of the noise for each pixel, we construct, for each of these pixels, a simulated image having a mean value equal to this level of noise, and compute its wavelet transform, the thresholds for each wavelet plane, and then replace by zero the wavelet coefficients which are lower than this threshold.

In order to estimate the noise level on each pixel, we will suppose that each pixel is in fact *entirely due to noise*. The obvious estimation of the noise level is then the value of the pixel itself. All we have to do then is, for each pixel value in the initial image, to simulate an image with noise having as a mean the pixel value itself. After computing the thresholds in the WPs of the simulated image, we compare them to the value of the wavelet coefficient in each WP of the initial image at the position of the pixel and see if the real values are lower than the threshold.

In fact, this method is conservative in the sense that it tests the hypothesis that *all the pixels in the real image are due to noise*. The value of a wavelet coefficient in a given WP at a certain position will result from the addition of the wavelet transform of all the pixels of the image. Locally, one assumes that the image is in fact a flat noisy image having a level equal to the pixel value (*that is what we assume in the simulated images*). If, surrounding a pixel, other pixels are not due to noise, their wavelet coefficient contribution at the position of the pixel will exceed the noise contribution, and the wavelet coefficient at the position of the pixel will be higher than the threshold measured in the simulations.

In practice, we don't take as the local noise estimation the value of the pixel itself, but the median value over a  $3 \times 3$  pixel square surrounding the pixel. This ensures that we don't have spurious zero-valued pixels surrounded by non-zero pixels. Second, we don't do a simulation for each pixel value of the image, but take the minimum and maximum values in the image, and choose  $N$  levels logarithmically between these two values (typically,  $N \sim 10$ ). We simulate  $N$  images with these  $N$  mean values and plot the threshold against the pixel value for each wavelet plane. We then fit the relation threshold-pixel value in each WP and use this fitted law to estimate the threshold in each WP for each pixel of the image. Fig. 1 shows this relation in logarithmic coordinates, as well as the fit.

## 2.5 Final image reconstruction

The final image reconstruction is a simple process of addition of the thresholded WPs. We don't iterate for this reconstruction, as this proves to be very time-consuming, without adding much information. We will show elsewhere (Dos Santos et al., in preparation) that this does not introduce important artefacts in the reconstructed image, although the hard-thresholding in the wavelet planes can sometimes cause changes of slopes in the reconstructed images, on the boundary from one scale to another.

## 2.6 Avoiding edge effects in the EUVE images

EUVE images exhibit the particular rectangular geometry of the detector. The fact that the length of one side greatly exceeds that of the other has proven to be a problem for the wavelet reconstruction algorithms, because the number density of counts goes rapidly to zero at the edge of the detector in one direction, but not in the other direction. In the wavelet planes, this large

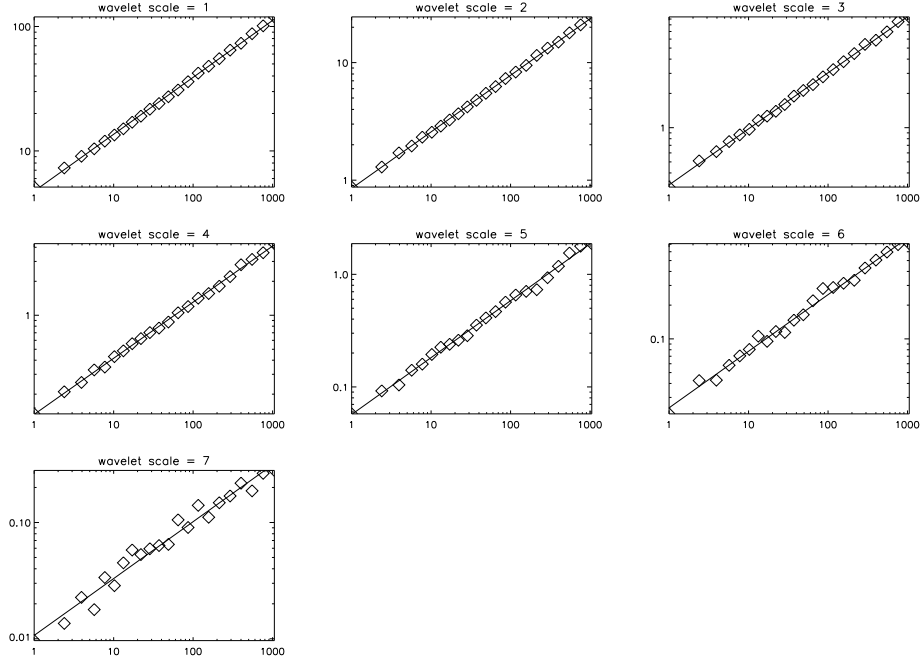


Figure 1: Fit of the WP thresholds as a function of the pixel value.

gradient translates in large wavelet coefficient values, particularly on the smallest scales. This in turn produces false object detections on a scale comparable to the photon count decrease.

The first simple idea to deal with this problem is to cut the image in order to have a comparable length and width, but the cluster emission is obviously truncated by this method, and the emission of all the clusters then doesn't extend further than 5 arcmin. This is obviously much smaller than detected by any classical analysis (*i.e.*, counts in radial bins), even the most conservative. We thus had to design a more complicated algorithm, in order to avoid false object detection without artificially limiting the extent of real cluster emission.

Fig. 2 shows the rebinned EUV image of the Virgo cluster. The cluster is clearly visible in the middle of the field of view. Three rotated rectangles are superimposed on the raw image. The largest one (ABCD) follows the outer detector shape closely; its edges are detached from the detector boundaries to avoid the steepening of the background near the edge, which would bias the noise estimation (see Fig. 2 of Lieu et al., 1999a). In this box, we define two rectangles (denoted  $r_1$  and  $r_2$ ), one on each side, as far away from the central source as possible. Both  $r_1$  and  $r_2$  are assumed to contain only noise and to be representative of the noise level. The second order moment of the count distribution is used to estimate the noise level in each of these rectangles. The noise level in the large box is then computed as the mean of the noise levels in both rectangles. Each pixel outside the larger box is then replaced by a random number drawn from a Poisson distribution, the variance of which is obtained by adding in quadrature the variances in each rectangle. The accuracy of the noise estimation is readily observable in the product image : if the noise is *underestimated*, the central box will obviously rise against the rest of the image, with its boundaries showing a clear discontinuity. On the other hand, if the noise has been *overestimated*, the outside parts of the new image rise against the central box, again showing a discontinuity on the boundaries. This particular technique allows us to recover a flat asymptotic background far from the center, a necessary condition for the good reconstruction and denoising of the image (Slezak et al., 1994). The wavelet-based reconstruction algorithm presented in the last section is applied to this newly created image.

When more than one EUVE observation of a cluster was available, we used the co-added

Figure 2: Virgo long exposure – definition of boxes in order to obtain the image ready for wavelet reconstruction. Note that the different boxes here are only illustrative of the algorithm we used.

Figure 3: A 1795 definition of boxes in order to obtain the image prior the wavelet reconstruction in the case of a co-added image.

image in order to increase the signal-to-noise ratio. Fig. 3 illustrates the case of A1795. This image is typical of the co-added images we dealt with in the case of other clusters. The difference in roll-angle of the satellite in both observations is apparent. The central intersection of both observations obviously has the highest signal-to-noise ratio. For each of the separate observations, we draw again a box that follows the outer detector shape closely. These boxes are labelled ABCD and A'B'C'D' in Figure 3. In each of the boxes, we define two rectangles, where the noise is evaluated. The noise level in a box is computed as the mean of the noise levels in both rectangles. Once this has been done for each box, each pixel outside the intersection of the boxes (the central diamond) is replaced by a random number drawn from a Poisson distribution, the variance of which is obtained by adding in quadrature the variances in each box. Once again, the under or overestimation of the noise will be clearly visible, and we apply to this image the reconstruction algorithm.

Obviously, we won't detect any structure outside a certain radius since the outer part of the image is made of pure noise. The central circle in Fig. 3 shows a conservative estimate of this radius ( $\sim 17$  arcminutes). We will thus compare X-ray and EUVE brightness profiles only inside this radius.

Dealing with ROSAT images does not present the same problems. The only geometrical complication arises from the presence at a radius of approximately 20 arcmin of the structure support of the telescope. This is not a big issue since the limiting radius obtained from the EUVE images is usually smaller than this value. When this is not the case (*e.g.* for Coma), this ring is taken as the limiting radius. On the other hand, what is of great concern here is the noise probability distribution function (hereafter PDF) after the data reduction. Indeed, the noise PDF is poissonian only in the raw counts detected by the PSPC, before Snowden's algorithms are applied. The exposure correction, as well as the subtraction of the different modelled backgrounds change drastically the noise PDF, which cannot be approximated any more by a Poisson process. Consequently, we have to take this fact into account in the reconstruction algorithm.

The images obtained after data processing are exposure-corrected and background-subtracted. We obtain the estimate of the various backgrounds (particle background, scattered solar X-ray background, ...) in sky coordinates, *i.e.*, in images with dimensions equal to those of the corrected image. An exposure image is also produced by the ESAS package. Adding the background files to the final image, we obtain a non-background-subtracted image. We need to run the ESAS package in order to have the background estimates, as well as the exposure maps in the different bands (which are summed after weighting by the total number of counts in each band). It is from this image that we compute our simulated images. Namely, as in the traditional reconstruction algorithm, we choose  $N$  levels between the minimum and the maximum pixel value of the image, and construct  $N + 1$  uniform images with a number of counts per pixel equal to each of these levels. Each of these images is then multiplied by the mean exposure map, and then only the Poisson noise is added to the simulated image (the noise is thus added to the non-exposure-corrected image, *thus simulating the observation before the data reduction*). After this, we divide the noisy simulated image by the mean exposure map and compute its

Table 2: Radius of the EUV and X-ray emissions derived from the wavelet reconstructed images. If the image is not circular, two numbers are given: the first is the horizontal (East-West) radius, the second the vertical (North-South) radius.

Cluster	EUV Radius (arcmin)	X-ray radius (arcmin)	EUV Radius (kpc)	X-ray radius (kpc)
A 1795	17	16	1800	1700
A 2199	$\geq 17$	18	$\geq 880$	940
A 4038	4.0-6.5	7.8-6.5	190-310	380-340
A 4059	7.4-5.7	17	600-460	1350
Virgo	$\geq 17$	18	$\geq 90$	100
Coma	$\geq 17$	20	$\geq 660$	780

Table 3: Kolmogorov Smirnov test on EUV and X-ray profiles: probability P that the profiles differ.

Cluster	P
A 1795	0.99940
A 2199	$(1 - 9 \cdot 10^{-10})$
A 4038	0.9990
A 4059	$(1 - 3 \cdot 10^{-8})$
Virgo	$(1 - 3 \cdot 10^{-6})$
Coma	0.1916

wavelet transform. The rest of the algorithm is analogous to that presented in section 2.4. This supplementary step in the construction of the simulated images allows us to simulate optimally the process of observation and data reduction of the ROSAT files.

### 2.7 Radial profiles

Once both (EUVE and ROSAT) images of a cluster were wavelet-reconstructed, we derived profiles from these 2D reconstructed images within elliptical concentric rings using the STSDAS.ANALYSIS.ISOPHOTE.ELLIPSE task in IRAF. For each cluster, the ellipticity and major axis position angle were first determined for the X-ray images, then fixed for both images, in order to compare the X-ray and EUV fluxes in the same spatial regions. Error bars on the profiles were computed by calculating the number of counts in each ring and taking as the error the square root of this number of counts.

## 3 Results

The maximum extents detected for the EUV and X-ray emissions are given in Table 2 for each cluster. The results of a Kolmogorov-Smirnov (hereafter K-S) test estimating for each cluster the probability that the EUV and X-ray profiles differ are given in Table 3.

The EUV and X-ray profiles for the six clusters are displayed in Figs. 4 to 9. The profile comparison for each cluster is briefly presented below.

The EUV and X-ray radii of A 1795 are 17 and 16 arcmin respectively (Fig. 4), corresponding to physical extents of 1800 and 1700 kpc. These extents are notably larger than previously found (Mittaz et al., 1998; Bonamente et al., 2001) and are by far the largest in all the sample (in physical units). The EUV and X-ray profiles appear to differ quite markedly, as confirmed by the K-S test, which gives a probability of 0.9994 that the two distributions are different (see Table 3).

The EUV and X-ray radii of A 2199 are 20 and  $\geq 17$  arcmin (our conservative limit, as

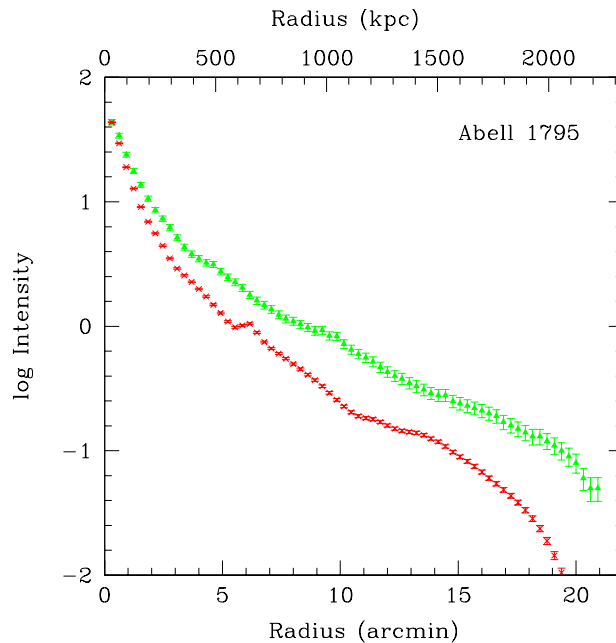


Figure 4: EUV (green triangles) and X-ray (red crosses) profiles for A 1795, with the radius expressed in arcminutes (bottom) and kpc (top) as in the five following figures.

explained in section 2.6) respectively (Fig. 5), or  $\geq 880$  and 940 kpc, larger than measured by Kaastra et al. (1999) both with EUVE and Beppo-Sax. Here also, the profiles differ with a very high probability.

A 4038 is located very close to a second EUV source, making it difficult to draw a profile for the EUV emission. We crudely modeled the EUV emission of this second source and subtracted it from the image, then deriving a profile for A 4038. This cluster is found to have the smallest radial extent in our sample, both in EUV and X-rays: 4.0-6.5 and 7.8-6.5 arcmin respectively (see Table 2 and Fig. 6). These values correspond to 190-310 and 380-340 kpc. This is the only cluster in our sample for which we used HRI data; due to the lower sensitivity of the HRI, it is not surprising that its X-ray emission is not detected very far from the center (less than 400 kpc in physical units). The EUV and X-ray profiles differ with a high probability.

In A 4059, the EUV and X-ray emissions reach 7.4-5.7 and 17 arcmin respectively (Fig. 7), somewhat larger than reported by Berghöfer et al. (2000a) and corresponding to 600-460 and 1350 kpc. The EUV and X-ray profiles differ with a very high probability.

Virgo is the coldest and most nearby cluster in our sample. EUV and X-ray emissions reach  $\geq 17$  and 18 arcmin respectively (Fig. 8), that is larger than previously detected (Lieu et al., 1996b; Berghöfer et al., 2000b; Bonamente et al., 2001); however, these extents correspond to the very small values of 90 and 100 kpc, due to the small redshift of Virgo. Here also, the EUV and X-ray profiles differ with a high probability.

The Coma cluster is the hottest cluster of our sample and behaves in a very different way. The EUV and X-ray radii reach  $\geq 17$  and 20 arcmin respectively (Fig. 9), somewhat larger than reported e.g. by Bowyer et al. (1999), and corresponding to  $\geq 660$  and 780 kpc respectively. The EUV and X-ray profiles appear to be very similar, at least in the inner 10 arcminutes, as confirmed by the K-S test; the probability that the two profiles differ varies with radius: it is low in the very center and becomes large further out, as illustrated in Table 4.

In order to compare all six clusters, the ratios of the EUV to X-ray intensities in concentric ellipses are shown in Figs. 10 and 11 for radii expressed in arcminutes and in kpc respectively.



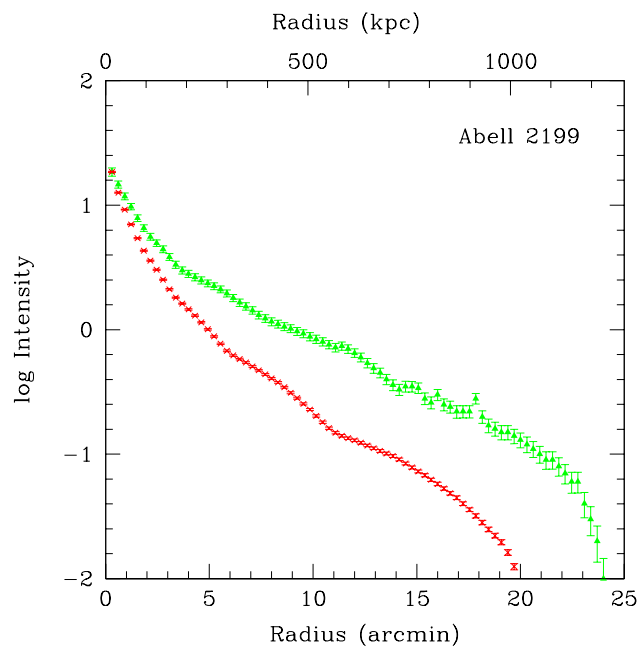


Figure 5: EUV and X-ray profiles for A 2199.

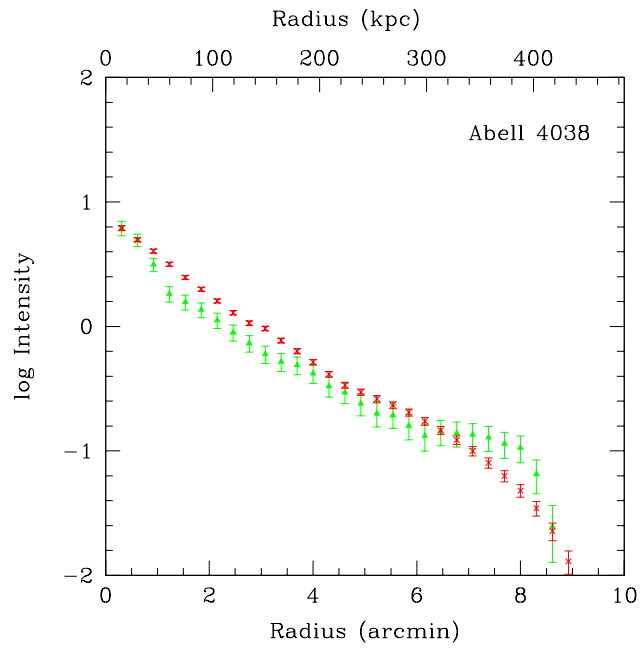


Figure 6: EUV and X-ray profiles for A 4038.

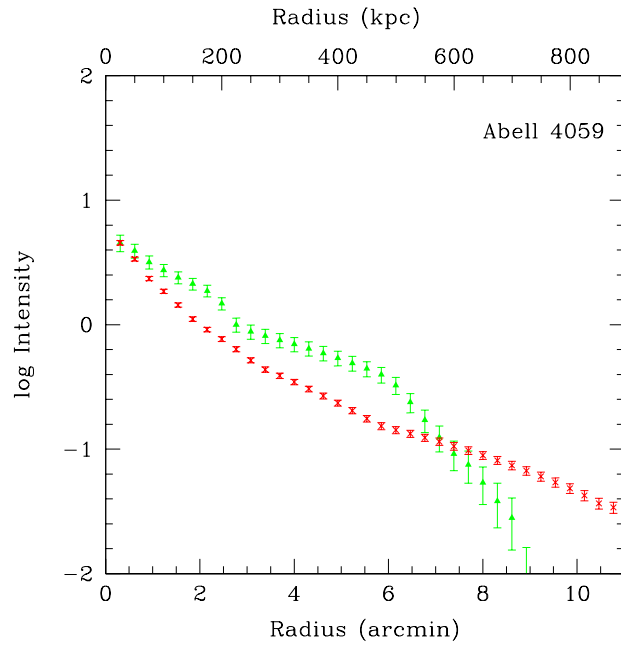


Figure 7: EUV and X-ray profiles for A 4059.

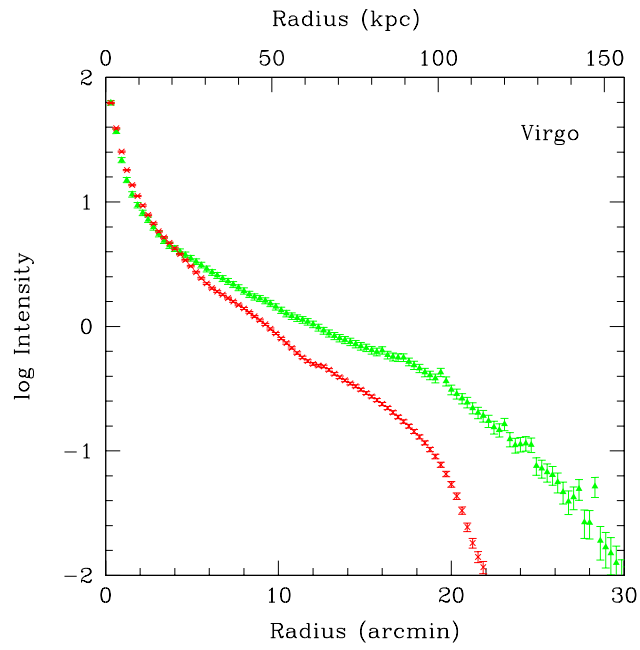


Figure 8: EUV and X-ray profiles for Virgo.

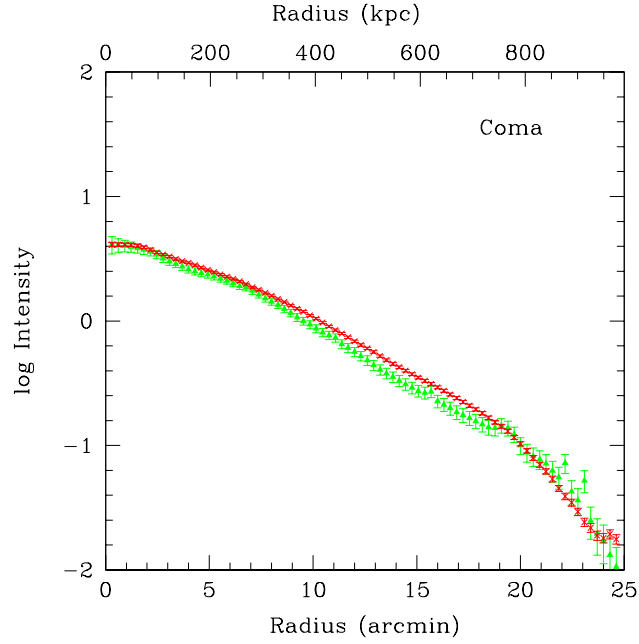


Figure 9: EUV and X-ray profiles for Coma.

Table 4: Kolmogorov Smirnov test on EUV and X-ray profiles of Coma: probability P that the profiles differ for concentric rings of various sizes.

Radius (arcmin)	P
$0 < R < 2$	0.0122
$2 < R < 17$	$(1 - 4.8 \cdot 10^{-11})$
$0 < R < 5$	0.1625
$5 < R < 17$	$(1 - 1 \cdot 10^{-9})$
$0 < R < 10$	0.5809
$10 < R < 17$	0.9999

## All clusters

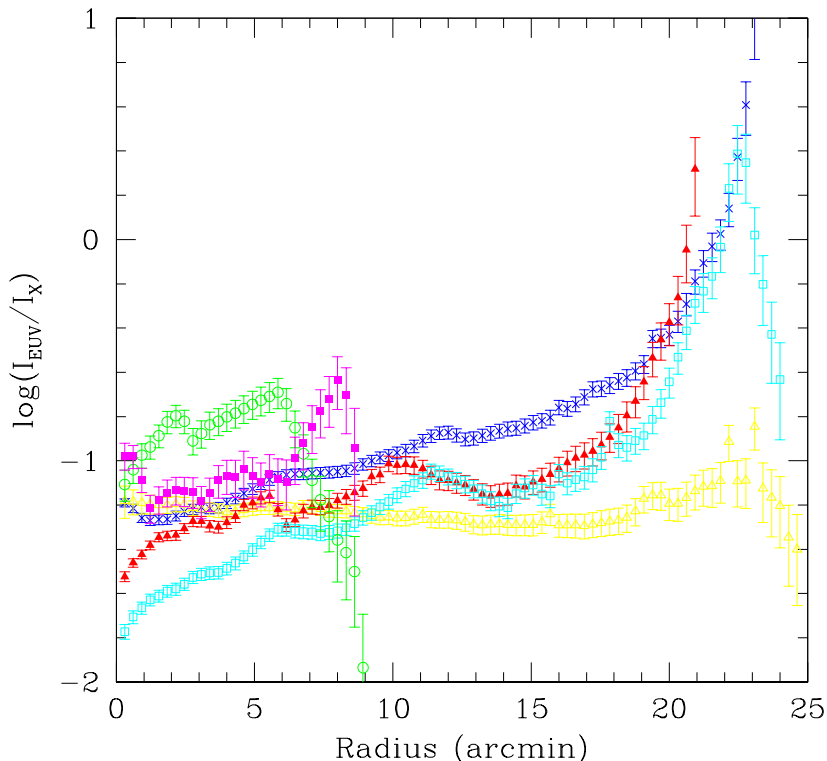


Figure 10: EUV and X-ray profiles for all six clusters in our sample, with the radius expressed in arcminutes. The following symbols are used: A 1795: filled red triangles; A 2199: empty light blue squares; A 4038: filled magenta squares; A 4059: empty green circles; Virgo: dark blue crosses; Coma: empty yellow triangles.

As mentioned above, we can see that four clusters out of six appear to extend both in the EUV and in X-rays at least up to 17 arcminutes, that is notably further than previously reported for EUV images. The two clusters which do not extend as far from the center (when the radii are expressed in arcminutes) are A 4038 and A 4059. This small physical extent is confirmed for A 4038 when the EUV to X-ray ratio is plotted in physical units (kpc). However, the physical extent of the EUV emission of A 4059 is 500-600 kpc, and therefore is not small.

On the other hand, the radial extent of the EUV and X-ray emission in Virgo is comparable to that of the other clusters when the radius is expressed in arcminutes, but becomes extremely small in physical units, due to the very small redshift of the cluster: slightly more than 100 kpc, that is of the order of the size of the central galaxy M87 (Böhringer et al., 2001).

## 4 Conclusions

The fact that the EUV and X-ray emission profiles markedly differ in five clusters out of the six of our sample clearly indicates that at least in these five clusters the EUV emission cannot be only due to the low energy tail of bremsstrahlung emission from the hot gas which accounts for the X-ray emission.

A test will obviously be to see if the existence of a soft EUV excess over bremsstrahlung emission from the hot X-ray emitting gas is confirmed by XMM.

## All clusters

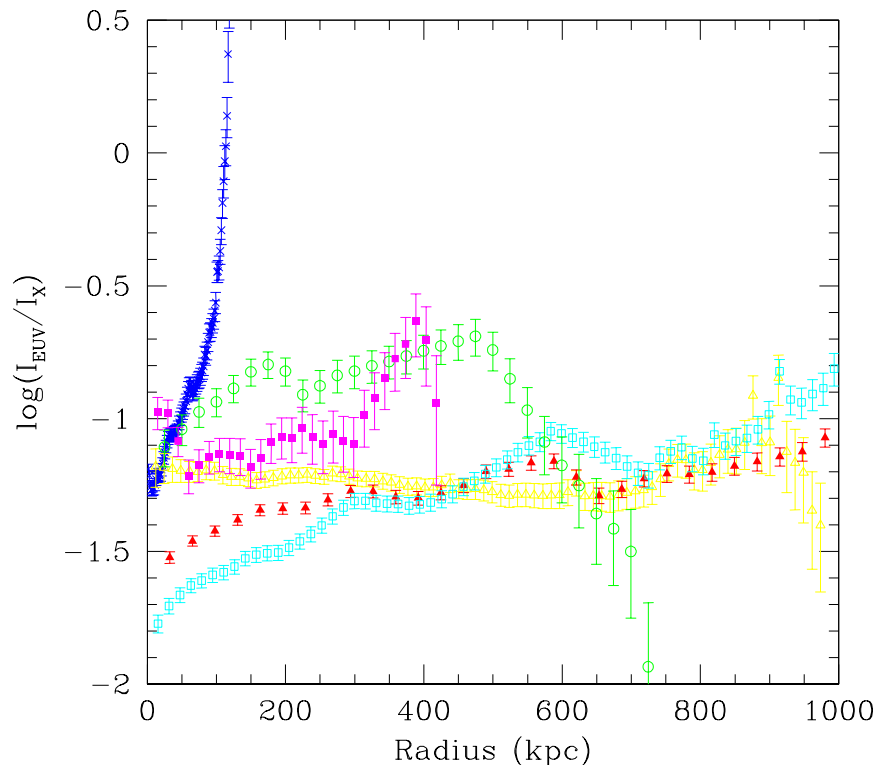


Figure 11: EUV and X-ray profiles for all six clusters in our sample, with the radius expressed in kpc.

## References

- Anscombe, F.J., 1948, *Biometrika* 15, 246
- Atoyan, A.M., Völk, H.J., 2000, *ApJ* 535, 45
- Berghöfer, T.W., Bowyer, S., Korpela, E., 2000a, *ApJ* 545, 695
- Berghöfer, T.W., Bowyer, S., Korpela, E., 2000b, *ApJ* 535, 615
- Böhringer, H., Belsole, E., Kennea, J., e.a., 2001, *A&A* 365, L181
- Bonamente, M., Lieu, R., Mittaz, J.P.D., 2001, *ApJ* 546, 805
- Bowyer, S., Berghöfer, T.W., 1998, *ApJ* 506, 502
- Bowyer, S., Berghöfer, T.W., Korpela, E.J., 1999, *ApJ* 526, 592
- Bowyer, S., Lieu, R., Mittaz, J.P., 1998, in: *IAU Symp. 188: The Hot Universe*, vol. 188, p. 185
- Brunetti, G., Setti, G., Feretti, L., Giovannini, G., 2001, *MNRAS* 320, 365
- Enßlin, T.A., Lieu, R., Biermann, P.L., 1999, *A&A* 344, 409
- Kaastra, J.S., Lieu, R., Mittaz, J.P.D., Bleeker, J.A.M., Mewe, R., Colafrancesco, S., Lockman, F.J., 1999, *ApJ* 519, L119

Lieu, R., Bonamente, M., Mittaz, J.P.D., 2001, ApJ , submitted astro-ph/0010610

Lieu, R., Bonamente, M., Mittaz, J.P.D., Durret, F., Dos Santos, S., Kaastra, J.S., 1999a, ApJ 527, L77

Lieu, R., Ip, W., Axford, W.I., Bonamente, M., 1999b, ApJ 510, L25

Lieu, R., Mittaz, J.P.D., Bowyer, S., Breen, J.O., Lockman, F.J., Murphy, E.M., Hwang, C., 1996a, Science 274, 1335

Lieu, R., Mittaz, J.P.D., Bowyer, S., Lockman, F.J., Hwang, C., Schmitt, J.H.M.M., 1996b, ApJ 458, L5

Mittaz, J.P.D., Lieu, R., Lockman, F.J., 1998, ApJ 498, L17

Murtagh, F., Starck, J.L., Bijaoui, A., 1995, Astronomy and Astrophysics Supplement Series 112, 179

Rué, F., 1996, Thèse de l'Université de Nice-Sophia Antipolis

Sarazin, C.L., Lieu, R., 1998, ApJ 494, L177

Shensa, M.J., 1992, Proceedings IEEE 40, 2464

Slezak, E., Bijaoui, A., Mars, G., 1990, A&A 227, 301

Slezak, E., Durret, F., Gerbal, D., 1994, AJ 108, 1996

Snowden, S.L., McCammon, D., Burrows, D.N., Mendehall, J.A., 1994, ApJ 424, 714

This figure "a1795\_boxes\_letters.jpg" is available in "jpg" format from:

<http://arxiv.org/ps/astro-ph/0105498v1>

This figure "virgonew\_box.jpg" is available in "jpg" format from:

<http://arxiv.org/ps/astro-ph/0105498v1>